



High-efficiency ultrathin porous phosphorus-doped graphitic carbon nitride nanosheet photocatalyst for energy production and environmental remediation

Daguang Li^a, Chenghui Wen^a, Jiaying Huang^b, Jiapeng Zhong^a, Ping Chen^a, Haijin Liu^c, Zhongquan Wang^a, Yang Liu^{b,*}, Wenying Lv^a, Guoguang Liu^{a,*}

^a School of Environmental Science and Engineering, Guangdong University of Technology, Guangzhou 510006, China

^b Guangdong Provincial Key Laboratory of Petrochemical Pollution Process and Control, School of Environmental Science and Engineering, Guangdong University of Petrochemical Technology, Maoming, Guangdong 525000, China

^c School of Environment, Henan Normal University, Key Laboratory for Yellow River and Huaihe River Water Environment and Pollution Control, Xinxiang 453007, China

ARTICLE INFO

Keywords:

g-C₃N₄
P doping
DFT calculations
NSAIDs degradation
H₂O₂ production

ABSTRACT

Herein, we designed and constructed an ultrathin porous phosphorus-doped g-C₃N₄ nanosheet (PCN) bifunctional photocatalytic system for efficient production of H₂O₂ and degradation of non-steroidal anti-inflammatory drugs in aqueous environment. The phosphorus atoms introduced in g-C₃N₄ significantly improved the utilization of light, enhanced the adsorption capacity for O₂, and inhibited the recombination of photogenerated carriers, thereby boosting the photocatalytic performance. Consequently, the optimized PCN photocatalyst produced 285.34 μM of H₂O₂ under blue LED light irradiation, which was 3.41 times that of pristine g-C₃N₄, and its degradation rate constant for diclofenac (0.1248 min⁻¹) was 46.22 times that of the g-C₃N₄. Density functional theory (DFT) calculations suggested that phosphorus doping modulated the local electronic structure of g-C₃N₄, which improved the electron-hole separation and promoted the O₂ reduction reaction. This work comprehensively reveals the mechanisms of phosphorus doping on g-C₃N₄, while offering a promising strategy for addressing current energy demands and environmental remediation concerns.

1. Introduction

With the increasingly rapid proliferation of industrialization and urbanization over the last few decades, the extensive deterioration of the ambient environment and increasing energy demands have emerged as two of the most serious challenges for humanity on a global scale [1]. Non-steroidal anti-inflammatory drugs (NSAIDs) are one of the most widely used classes of pharmaceuticals worldwide [2]. Although most NSAIDs have a short half-life, they continue to permeate the aquatic environment due to frequent human use and the inadequate discharge protocols of some factories. It has been reported that NSAIDs are widely detected in sewage and surface water, with concentrations reaching ng L⁻¹ ~ μg L⁻¹ levels [3,4]. Recent investigations have revealed that NSAID molecules with high biological activity may convey potential toxicity to non-target organisms in aqueous ecosystems and human health [5]. Due to the currently insufficient removal of NSAIDs in

wastewater treatment plants (WWTPs) via traditional treatment processes [6], there is an urgent need to develop robust, effective, and sustainable NSAIDs treatment technologies.

Hydrogen peroxide (H₂O₂) is a green and clean energy source, as its only by-products are oxygen and water. It not only possesses the advantages of high energy density and convenient storage, but can also be utilized to generate electricity in one-compartment fuel cells, which is considered an ideal substitute for hydrogen and other fuel gases [7,8]. It is worth noting that in addition to being extensively employed in bleaching, disinfection, and chemical synthesis, H₂O₂ is also used for environmental remediation. Since the hydroxyl radicals (•OH) converted by the H₂O₂-based advanced oxidation process have an extremely high oxidation potential, they can non-selectively degrade or even mineralize organic pollutants [9–11]. Nevertheless, conventional H₂O₂ production technologies such as the standard anthraquinone process [12], cathodic oxygen reduction method [13], and direct H₂/O₂

* Corresponding authors.

E-mail addresses: liuyang@gdpu.edu.cn (Y. Liu), liugg615@163.com (G. Liu).

<https://doi.org/10.1016/j.apcatb.2022.121099>

Received 12 August 2021; Received in revised form 10 January 2022; Accepted 13 January 2022

Available online 15 January 2022

0926-3373/© 2022 Published by Elsevier B.V.

synthesis [14], have issues with high energy consumption, high production costs, and potential explosion risks, which limits its widespread application [15,16].

Semiconductor-based photocatalysts can utilize solar energy to activate molecular oxygen for the generation of reactive oxygen species, which is an attractive two-in-one strategy for the degradation of organic pollutants and production of H_2O_2 . Among them, graphitic carbon nitride (g-C₃N₄), as a metal-free conjugated polymer with a band gap of ~ 2.7 eV, has emerged as one of the ideal candidates [17–19]. Generally, during the g-C₃N₄ photocatalytic process, H_2O_2 may be produced via indirect successive two-step single-electron reduction ($\text{O}_2 \rightarrow \text{O}_2^{\cdot-} \rightarrow \text{H}_2\text{O}_2$), or direct one-step two-electron reduction ($\text{O}_2 \rightarrow \text{H}_2\text{O}_2$) [20,21]. Further, the generated superoxide radicals ($\text{O}_2^{\cdot-}$) and $\cdot\text{OH}$ have sufficient oxidizing power and can be employed to degrade organic pollutants. Obviously, the yield of these active oxygen species is highly dependent on the generation and migration of photo-generated electrons as well as the O_2 adsorption capacity of the catalyst surface. However, bulk g-C₃N₄ still suffers from unsatisfactory photocatalytic efficiencies due to its low specific surface area, inadequate optical absorption, and rapid recombination of photogenerated electrons and holes [22,23].

Consequently, various modification strategies have been adopted to improve the photocatalytic activities of bulk g-C₃N₄ [24–26]. For example, the synthesis of ultra-thin porous g-C₃N₄ nanosheets can greatly enhance the specific surface area, while significantly increasing the population of reaction sites [27,28]. Another important approach is through chemical doping, particularly doping with non-metal elements. Among these, extensively studied P-doped g-C₃N₄ exhibits the advantages of high efficiency, facile preparation procedure, superior physicochemical stability, and favorable environmental compatibility [29,30]. According to previous work, the introduction of a lower proportion of P atoms can significantly augment the utilization of light, reduce the band gap, while inhibiting the recombination of electron-hole pairs [31,32]. However, the impacts of P-doping on the molecular structural changes of g-C₃N₄ and the separation of photogenerated electron-hole pairs have rarely been investigated. The comprehensive investigation of these aspects can facilitate a deep understanding of the mechanisms of P-doping, while providing a theoretical basis for the application of P-doped g-C₃N₄. Furthermore, to the best of our knowledge, there are no reports to date on the simultaneous application of P-doped g-C₃N₄ for energy production and water decontamination.

For this study, an ultrathin porous P doped g-C₃N₄ nanosheet (PCN) was successfully synthesized through a one-step thermal polymerization method. The morphological structure, optical, and electrochemical properties of the PCN were investigated. Importantly, density functional theory (DFT) calculations were conducted to elucidate their electronic structures and reveal the separation of photogenerated carriers. As anticipated, the PCN photocatalyst exhibited superior photocatalytic performance for the production of H_2O_2 and degradation of NSAIDs under blue LED light irradiation. Moreover, the H_2O_2 formation route over PCN was revealed via electrochemical workstation and rotating disk electrode (RDE) measurements. The generation of reactive species and the photocatalytic degradation mechanisms were explored through electron spin resonance (ESR) and quenching experiments. We also evaluated the feasibility of a PCN photocatalytic system in actual aquatic environments, including the impacts of water quality parameters and natural water matrices. Ultimately, the transformation products of diclofenac (DCF, a typical NSAID) and degradation pathways were determined via UPLC-Q-TOF MS analysis.

2. Experimental section

2.1. Chemical reagents

The reagents and ultrapure water used in the experiments are given in Text S1, Supplementary Material.

2.2. Preparation of photocatalysts

Ultrathin porous phosphorus doped g-C₃N₄ nanosheet (PCN) was synthesized via a one-step thermal polymerization method [18]. Briefly, 1 g of dicyandiamide, 5 g of ammonium chloride (NH_4Cl), and different quantities of 1-Hydroxyethylidene-1,1-diphosphonic acid (HEDP) were thoroughly ground in an agate mortar for five minutes, and then annealed in a muffle furnace at 550 °C for 4 h at a ramp rate of 2 °C min⁻¹. Once cooled to room temperature, the products were rinsed several times with ultrapure water, and finally dried at 60 °C for 12 h. The samples were denoted as xPCN, where x (x = 35, 50, and 75) represented the milligrams of HEDP added to the raw material. Moreover, the accurate doping amounts of P element in 35PCN, 50PCN, and 75PCN determined by the inductively coupled plasma-optical emission spectrometry (ICP-OES) were 0.18, 0.48, and 1.03 wt%, respectively. For comparison, the porous g-C₃N₄ nanosheet (CNN) was similarly prepared via the above method without the addition of HEDP. The phosphorus doped g-C₃N₄ (CNP) was prepared without adding NH_4Cl , and the pristine g-C₃N₄ (CN) was obtained without the addition of NH_4Cl and HEDP.

2.3. Characterization of photocatalysts

The characterization methods of as-prepared photocatalysts are displayed in Text S2, Supplementary Material.

2.4. Photocatalytic reactor and optical properties of catalyst suspension

The photocatalytic experiments were carried out in a hollow cylindrical quartz tube photoreactor as shown in Fig. S1a. The light source was provided by a 9 W blue LED lamp with a wavelength range of 410–530 nm (Fig. S1b) (Shenzhen Lamplic Technology Co., China). A circulating water bath was employed to maintain the reaction temperature at 25.0 °C.

The extinction coefficients β_λ of catalyst aqueous suspensions with different concentrations were determined by the UV–vis spectrophotometer.

$$\beta_\lambda = \frac{2.303ABS_\lambda}{L} \quad (1)$$

Where ABS_λ is the absorbance and L is cell length in the unit of cm.

The specific extinction coefficient β_λ^* ($\beta_\lambda^* = \beta_\lambda / C_{\text{cat}}$) was calculated using linear regression on the data and enforcing a zero intercept, which is the sum of the specific absorption coefficient κ_λ^* and the specific scattering coefficient σ_λ^* [33]:

$$\beta_\lambda^* = \kappa_\lambda^* + \sigma_\lambda^* \quad (2)$$

Furthermore, the infinite reflectance value R of the catalyst solid was measured by UV–vis DRS spectra. Based on the Kubelka-Munk function, $F(R)$ can be calculated as follows to determine the ratio of κ_λ^* and σ_λ^* [34]:

$$F(R) = \frac{(1-R)^2}{2R} = \frac{\kappa_\lambda^*}{\sigma_\lambda^*} \quad (3)$$

Consequently, κ_λ^* and σ_λ^* can be determined by combining Eqs. (2) and (3).

The spectral-averaged specific absorption and scattering coefficients κ^* and σ^* of catalysts were determined by averaging κ_λ^* and σ_λ^* over the useful spectrum of the incident irradiation (I_λ) [34,35]:

$$\kappa^* = \frac{\int_{\lambda_{\min}}^{\lambda_{\max}} \kappa_\lambda^* I_\lambda d\lambda}{\int_{\lambda_{\min}}^{\lambda_{\max}} I_\lambda d\lambda} \quad (4)$$

$$\sigma^* = \frac{\int_{\lambda_{\min}}^{\lambda_{\max}} \sigma_{\lambda}^* I_{\lambda} d\lambda}{\int_{\lambda_{\min}}^{\lambda_{\max}} I_{\lambda} d\lambda} \quad (5)$$

where λ_{\min} and λ_{\max} are respectively the minimum and maximum wavelengths of the incident radiation that can be absorbed by the photocatalyst.

For a planar geometry, the optical thickness τ is defined as follows [36]:

$$\tau = (\kappa^* + \sigma^*) C_{\text{cat}} \delta \quad (6)$$

Where C_{cat} is the concentration of the catalyst and δ is the characteristic length for the extinction of the light inside the reactor.

2.5. Evaluation of photocatalytic H_2O_2 production

During each photocatalytic test, 50 mg of the catalysts were dispersed in a mixed solution containing 45 mL of ultrapure water and 5 mL of ethanol. Subsequently, the mixture was purged through oxygen bubbling for 30 min and then magnetically stirred in the dark for 30 min to ensure oxygen saturation and adsorption-desorption equilibrium. During the light-driven reaction, 1.5 mL of the suspension were extracted at predetermined time intervals and filtered through 0.45 μm Millipore filters to remove the catalyst. The quantity of generated H_2O_2 was determined by iodometry [37]. Typically, 0.75 mL of a 0.1 M potassium hydrogen phthalate aqueous solution and 0.75 mL of iodide reagent (containing 0.4 M potassium iodide, 0.06 M NaOH, and 10^{-4} M ammonium molybdate) were added to the obtained solution, and kept for 30 min. The absorbance at 350 nm was detected using a UV-3200 spectrophotometer (Mapada Instruments, China). The concentration of H_2O_2 was calculated using the equation shown in the working curve (Fig. S2).

2.6. Evaluation of photocatalytic NSAIDs degradation

Diclofenac was selected as the representative NSAIDs pollutant to evaluate the photocatalytic performance of the samples under blue LED irradiation. In a typical experiment, 20 mg of the samples were dispersed in 50 mL of a DCF aqueous solution (10 mg L^{-1}), after which the mixture was magnetically stirred in dark for 30 min to achieve adsorption-desorption equilibrium. During light irradiation, 1 mL of the reaction solution was extracted at specific time intervals and immediately filtered for analysis. The residual concentrations of NSAIDs were measured by high performance liquid chromatography (HPLC, Shimadzu Co., Japan), whereas the degradation intermediates of the DCF were identified by ultra-high performance liquid chromatography combined with quadrupole time-of-flight mass spectrometry (UHPLC-Q-TOF-MS). Detailed information on these instruments is provided in Text S3, Text S4, and Table S1. Further detailed information on the determination of reactive species is given in Text S5.

2.7. Theoretical calculations

The methods and details of theoretical calculations are provided in Text S6, Supplementary Material.

3. Results and discussion

3.1. Morphology and structure

The morphologies of as-prepared photocatalysts were revealed through SEM and TEM analyses. Fig. S3a depicts a SEM image of bulk CN, which exhibited a typical blocky stacked structure. Compared with the CN, the morphologies of CNN and 50PCN were significantly altered, becoming a fragmented and richly porous structure (Figs. S3b, c). The formation of this hierarchical pore structure was due to the

decomposition of NH_4Cl to gaseous NH_3 and HCl at high temperatures, which served as soft templates during the dicyandiamide condensation process [25]. The TEM images (Fig. 1a and S4) confirmed the transformation from the thick CN to the thin and porous 50PCN. Atomic force microscopy (AFM) was performed to further study the structural features of the nanosheets. AFM image and the corresponding height profile (Fig. S5) revealed that the average thickness of the 50PCN nanosheet was $\sim 12 \text{ nm}$, which was 7.1 times thinner than that of the CN. The elemental mapping images shown in Fig. 1b reveal the uniform distribution of the three component elements (C, N, and P) in the 50PCN.

Fig. 1c illustrates the N_2 adsorption-desorption isotherms of the CN, CNN, CNP, and 50PCN. The 50PCN displayed a type IV isotherm with distinct H3 hysteresis loops. Furthermore, the pore size distribution curve (Fig. 1c inset) confirmed the mesoporous structure of the 50PCN. As expected, the BET surface area of the CNN and 50PCN were 48.239 and $73.850 \text{ m}^2 \text{ g}^{-1}$, respectively, which were far higher than that of the CNP ($16.981 \text{ m}^2 \text{ g}^{-1}$) and CN ($5.982 \text{ m}^2 \text{ g}^{-1}$). The XRD patterns of the as-synthesized CN, CNN, CNP, 35PCN, 50PCN, and 75PCN are depicted in Fig. 1d. As previously reported, the CN exhibited two typical diffraction peaks at 13.0° and 27.4° , which were indexed as the (100) and (002) planes of g- C_3N_4 , respectively [38]. In contrast to the CN, the XRD patterns of xPCN samples showed similar characteristics, except that their (100) and (002) peaks were significantly weaker. The FT-IR spectra of the CN, CNN, CNP, and xPCN are shown in Fig. S6. All of the samples exhibited similar characteristic vibration modes, which suggested the good retention of the tri-s-triazine-based structure of g- C_3N_4 in CNN, CNP, and xPCN [39].

XPS was employed to investigate the surface composition and chemical states of the CN and 50PCN. As illustrated in the survey spectra (Fig. 2a), the 50PCN was comprised of C, N, O, and P. In the C1s spectra (Fig. 2b), both the CN and 50PCN exhibited three main peaks at 284.8, 286.4, and 288.2 eV, which represented C-C, C-O, and N=C-N, respectively. The N1s spectra (Fig. 2c) of the CN and 50PCN were divided into three peaks at approximately 398.6, 400.1, and 401.2 eV, which were ascribed to C=N-C, N-(C)₃, and NH_x , respectively [26]. The P 2p spectrum (Fig. 2d) of the 50PCN could be fitted into a peak at 133.5 eV, which was attributed to P-N, whereas the CN displayed no detectable signal from phosphorus. Notably, the results of elemental analysis (Table S2) revealed that the C/N atomic ratio of the 50PCN was 0.538, which was lower than that of the CN (0.563), indicating the partial deletion of C atoms. Also, an increase in the NH_x content of the 50PCN in the N1s XPS spectra further confirmed the formation of carbon defects [20,40]. Moreover, Fig. 2e shows the solid-state ^{13}C NMR spectra of the CN and 50PCN. They both exhibited the same signals at $\sim 156.8 \text{ ppm}$ and 164.7 ppm , which were assigned to CN_3 and CN_2NH_2 groups, respectively [41]. As depicted in Fig. 2f, the solid-state ^{31}P NMR spectrum of the 50PCN had two well-resolved signals between 40.0 and -20.0 ppm , which corresponded to two different chemical environments of P in the framework structure [30]. These results indicated that P was likely to replace the corner or bay carbon in the triazine rings, accompanied by the generation of carbon defects. For the following theoretical research, a bulk PCN model (PCN_bulk) was designed as shown in Fig. 1e. The optimized lattice constant was 13.67 Å and layer space was 3.21 Å, which coincided with those of the XRD experiments (13.60 Å and 3.25 Å). Similar model was also observed in previous reports by Guo et al. [42].

3.2. Optical and photoelectrochemical properties

As can be seen in Fig. 3a, the CN exhibited a typical absorption edge at $\sim 458 \text{ nm}$, while the 50PCN possessed an extended absorption edge at $\sim 492 \text{ nm}$, and its light absorption was significantly enhanced. The EPR spectra (Fig. 3b) showed that both the CN and 50PCN displayed a paramagnetic signal with a g value of 2.003, which corresponded to unpaired electrons within the π -conjugated aromatic rings [43]. Obviously, this EPR signal in the 50PCN was significantly enhanced

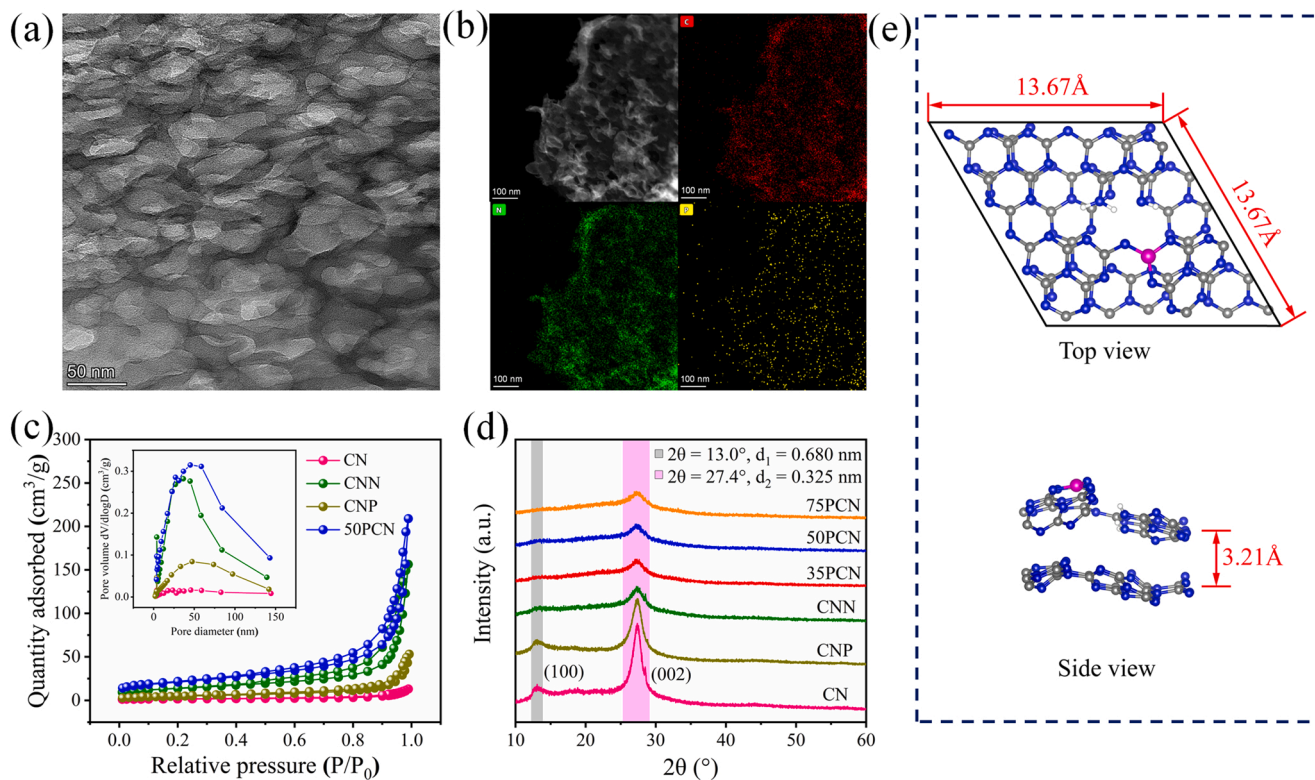


Fig. 1. (a) TEM image, and (b) elemental mapping images of the 50PCN. (c) N₂ adsorption-desorption isotherms and the corresponding pore size distribution curves (insert) of the CN, CNN, CNP, and 50PCN. (d) XRD patterns of the as-prepared samples. (e) Top view and side view of optimized PCN_bulk.

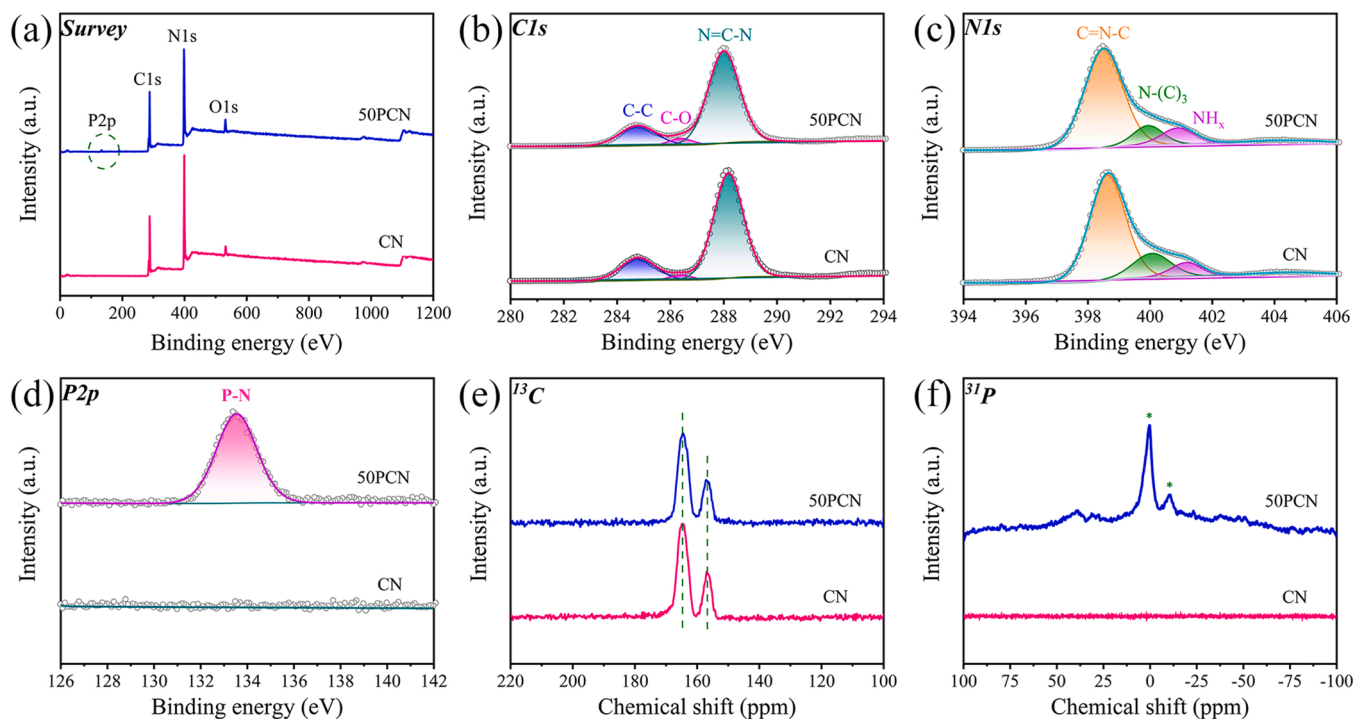


Fig. 2. (a) Full surface survey XPS spectra; high-resolution XPS spectra of (b) C 1s, (c) N 1s, and (d) P 2p; (e) solid-state ¹³C NMR spectra, and (f) solid-state ³¹P NMR spectra of the CN and 50PCN.

compared with the CN, which indicated a higher concentration of unpaired electrons that was significantly beneficial for the separation and transfer of photogenerated carriers during the photocatalytic reaction.

Fig. 3c shows the steady-state PL spectra of the CN and 50PCN. The

fluorescence intensity of the 50PCN was much lower than that of the CN, which indicated that the recombination of photogenerated carriers was effectively inhibited [44]. Furthermore, time-resolved fluorescence decay spectroscopy was performed on the CN and 50PCN to quantify the

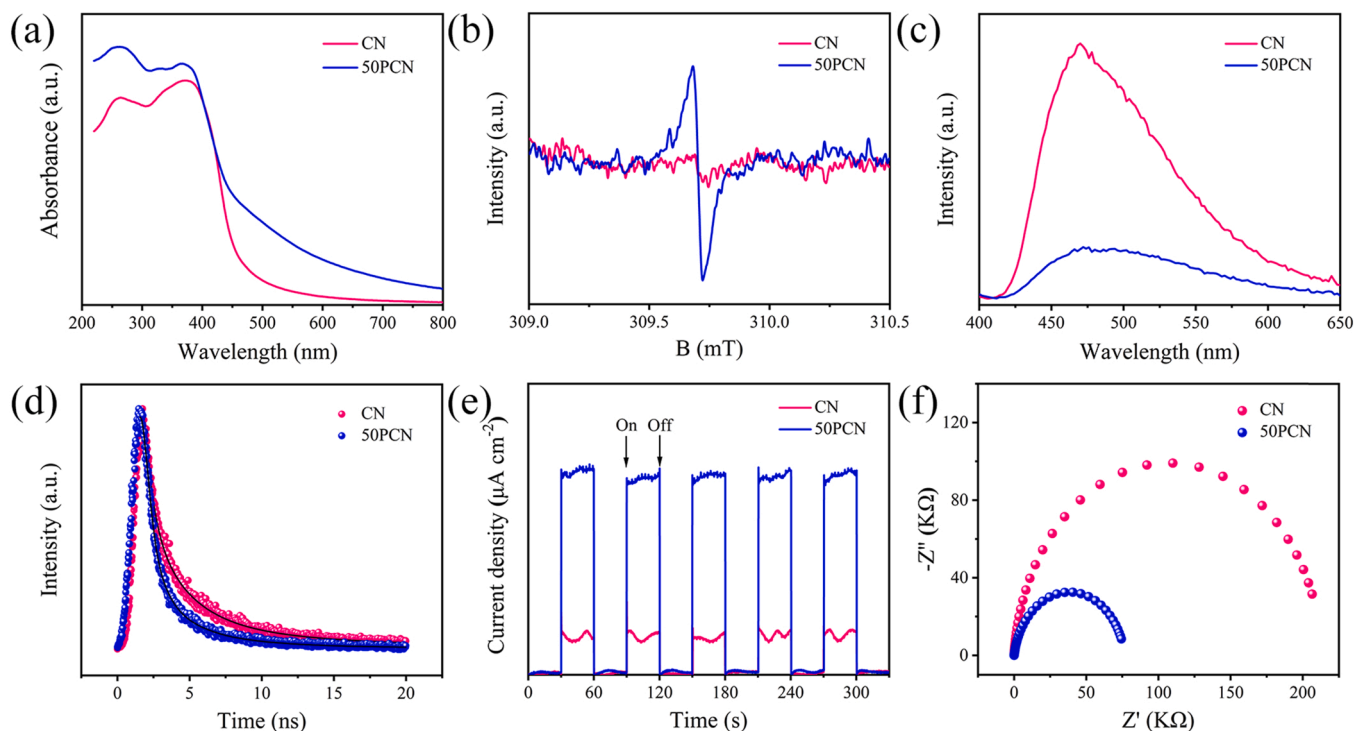


Fig. 3. (a) UV–vis absorption spectra, (b) room temperature EPR spectra, (c) steady-state photoluminescence spectra, (d) time-resolved photoluminescence decay spectra, (e) transient photocurrent density response curves, and (f) EIS Nyquist plots of the CN and 50PCN.

lifetimes of the charge carriers (Fig. 3d). The detailed information and data results of the fitting method are given in Text S7 and Table S3. Consequently, the average radiative lifetimes of the CN and 50PCN were 4.68 and 2.26 ns, respectively. The reduced decay lifetime and quenched PL suggested more effective charge carrier formation and faster charge transfer in the 50PCN [45,46]. Moreover, Fig. 3e, f show the transient photocurrent response curves and electrochemical impedance spectra of the CN and 50PCN. Compared with the CN, the 50PCN demonstrated a greatly enhanced photocurrent intensity and smaller impedance, which confirmed that the photogenerated carriers

recombination was greatly inhibited and the charge transfer was effectively improved [47,48].

3.3. Density functional theory (DFT) calculations

To elucidate the photoinduced electron transfer mechanisms of the PCN, a detailed theoretical study was conducted. We created a bulk PCN model (PCN_bulk, two layers, a P-doped layer with carbon defect, and a CN layer) (Fig. 1e). As can be seen from the VBM (valence band maximum) and CBM (conduction band minimum) of PCN_bulk (Fig. S7),

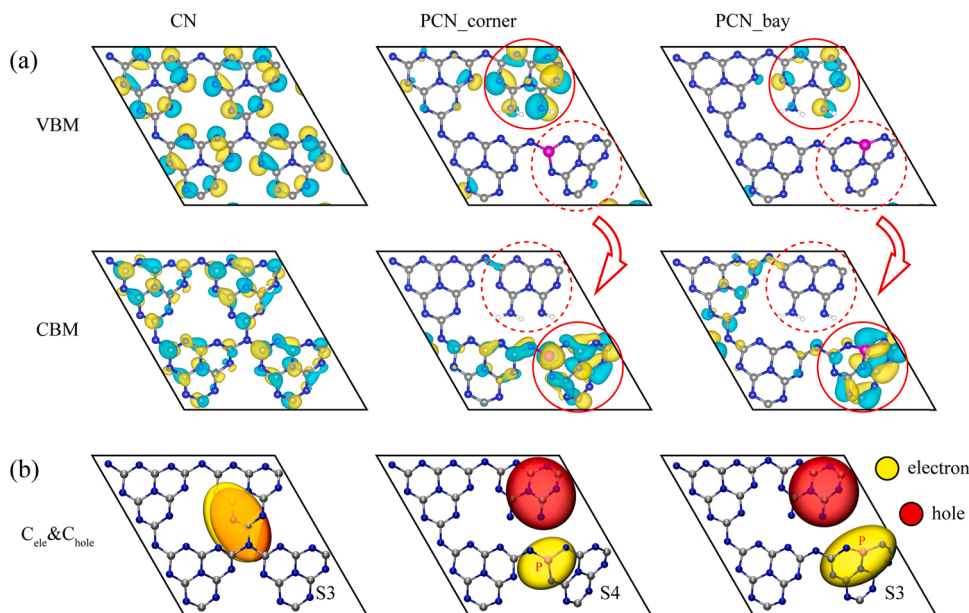


Fig. 4. (a) Wavefunction contour maps of VBM and CBM for the CN, PCN_corner, and PCN_bay. (b) Contour maps of C_{ele} and C_{hole} for $S_0 \rightarrow S_3$ of the CN, $S_0 \rightarrow S_4$ of the PCN_corner, and $S_0 \rightarrow S_3$ of the PCN_bay.

the main contributor was the P-doped layer with carbon defects. Thus, we selected the P-doped layer with carbon defects as the DFT research object. Because of two potential doping sites (corner C site and bay C site) for P atoms, both the corner PCN (PCN_corner) and bay PCN (PCN_bay) were inspected.

As depicted in Fig. 4a, all sites contributed equally to the VBM and CBM for the CN; however, the carbon defect sites contributed primarily to the VBM, and the P-doped sites contributed significantly to the CBM for PCN_corner and PCN_bay. Hence, it appeared that the excitation types were remarkably altered subsequent to P doping. Further, electron-hole analysis was performed to investigate the characteristics of electron excitation. As the main contributed molecular orbitals for $S_0 \rightarrow S_3$ (CN), $S_0 \rightarrow S_4$ (PCN_corner) and $S_0 \rightarrow S_3$ (PCN_bay) were HOMOs and LUMOs, their excitation types had a strong influence on the photoinduced characteristics of the CN, PCN_corner, and PCN_bay. The highly separated contour map centers of C_{ele} and C_{hole} (yellow iso-surfaces, red isosurfaces) (Fig. 4b), the large values of D_{index} , low values of $S_{r,\text{index}}$, and positive values of t_{index} (Table 1) verified that the excitation types of $S_0 \rightarrow S_4$ (PCN_corner) and $S_0 \rightarrow S_3$ (PCN_bay) were charge-transfer excitation (CT). The excitation type of $S_0 \rightarrow S_3$ (CN) was local excitation (LE). Besides, the other excited states ($S_0 \rightarrow S_4$) of the CN, PCN_corner, and PCN_bay were also investigated (Fig. S8 and Table S4). C_{ele} & C_{hole} , D_{index} , $S_{r,\text{index}}$, and t_{index} are elaborated in the supplementary material. Overall, the separation of electrons and holes in PCNs was much better than in CN, while the recombination of electrons and holes in PCNs was more difficult than in CN. Additionally, electron localization function (ELF) analysis indicated that the electrons on P-doped sites were easily delocalized to other regions (Fig. S9), whereas electrostatic potential analysis verified that the capacity to lose electrons for the CN was enhanced after P doping (Fig. S10). All of the above results suggested that P doping was favorable for the generation of photoinduced carriers and restrained their recombination.

3.4. Photocatalytic production of H_2O_2

The photocatalytic production of H_2O_2 proceeded in an O_2 -saturated ethanol aqueous solution (10 vol%) under blue LED light irradiation. The generation of H_2O_2 was detected by UV-vis absorption spectroscopy, and the absorption at 350 nm gradually increased with longer irradiation times (Fig. S11). As shown in Fig. 5a, H_2O_2 could scarcely be detected in the absence of photocatalysts, while the 50PCN showed the best photocatalytic activity. The amount of H_2O_2 generated on the 50PCN attained 285.34 μM following 180 min of illumination, which was 3.41 times that of the CN (83.76 μM), and was higher than that of most carbon nitride-based materials reported previously (Table S5). Meanwhile, under the same experimental conditions, the 50PCN produced the largest amount of H_2O_2 , compared with the O doped CN, defective CN, commercial P25 and commercial MoS_2 (Fig. S12). These results indicated that the 50PCN showed tremendous advantages in H_2O_2 production after modification with porous structure and P doping. Nevertheless, the photocatalytic activity of 75PCN for H_2O_2 production decreased slightly, which might have been attributed to excessive P doping that provided new recombination sites for photogenerated carriers.

Several control experiments of photocatalytic H_2O_2 production were carried out with the CN and 50PCN. As shown in Fig. S13, under a N_2 atmosphere, the yield of H_2O_2 generated by the CN and 50PCN was close to zero, which suggested that these photocatalytic systems could not

produce H_2O_2 without O_2 . Moreover, to examine the O_2 adsorption capacities of the photocatalysts, the temperature-programmed desorption of O_2 (O_2 -TPD) was conducted (Fig. S14). There was practically no oxygen desorption peak in the CN, while the 50PCN displayed two oxygen desorption peaks at 155 $^\circ\text{C}$ and 460 $^\circ\text{C}$. These results indicated that the 50PCN exhibited a stronger adsorption capacity for O_2 , which contributed to the generation of additional reactive oxygen species.

In addition, without the addition of ethanol, the quantity of H_2O_2 generated by the photocatalysts was drastically reduced (Fig. S13). The 50PCN produced 37.55 μM of H_2O_2 , while the CN produced only 4.14 μM within 180 min. This was because ethanol reacted with photogenerated holes to enhance charge separation and provided protons for the generation of H_2O_2 [19,49]. The comparison of the photocatalytic H_2O_2 production of different catalysts without sacrificial agent was also listed in Table S5. Moreover, linear sweep voltammetry (LSV) curves demonstrated that the 50PCN also exhibited better oxygen reduction reaction (ORR) performance compared to other carbon nitride-based catalysts reported in the literature (Fig. S15). A cyclic experiment was conducted to evaluate the stability of the 50PCN for the production of H_2O_2 (Fig. 5b). The photocatalytic activity of the 50PCN for the generation of H_2O_2 decreased only slightly after four cycles, which suggested that the photocatalyst was stable and reusable. Typically, the photocatalytic production of H_2O_2 also depends on the pH value of the reaction system. As shown in Fig. 5c, acidic conditions were favorable for the light-driven generation of H_2O_2 . However, under higher pH, the amount of H_2O_2 production decreased rapidly, likely because protons were greatly reduced in an alkaline solution.

The ORR pathway was investigated using electrochemical rotating disk electrode (RDE) analysis. Fig. S16 depicts the LSV curves of the CN and 50PCN in an O_2 -saturated 0.5 M H_2SO_4 solution at different rotation speeds. The transfer electron number (n) involved in the O_2 reduction was determined based on Koutecky-Levich equations (Eqs. 7 and 8):

$$j^{-1} = j_k^{-1} + B^{-1}\omega^{-1/2} \quad (7)$$

$$B = 0.2nFCD^{2/3}\nu^{-1/6} \quad (8)$$

Where j and j_k are the measured current density and the kinetic current density, ω is the electrode rotating speed (rpm), F is the Faraday constant (96485 C mol $^{-1}$), C is the bulk concentration of O_2 , D is the diffusion coefficient of O_2 in 0.5 M H_2SO_4 (1.93×10^{-5} cm 2 s $^{-1}$), and ν is the kinetic viscosity of the electrolyte (1.009×10^{-2} cm 2 s $^{-1}$) [50]. As illustrated in Fig. 5d, the n values of the CN and 50PCN calculated from the slope of the Koutecky-Levich plots were 1.52 and 1.65, respectively. Notably, the n values of the CN and PCN were both less than 2, indicating that they mainly generated H_2O_2 through sequential two-step single-electron O_2 reduction. In addition, the generation of $\text{O}_2^{\bullet-}$ was investigated by ESR technique using DMPO as the spin-trapping agent (Fig. 6d). Both the CN and 50PCN exhibited the signal of DMPO- $\text{O}_2^{\bullet-}$, but the DMPO- $\text{O}_2^{\bullet-}$ signal of 50PCN was significantly higher than that of CN, which indicated that the introduction of P atoms can promote the $\text{O}_2^{\bullet-}$ generation. Furthermore, there was almost no H_2O_2 generation when the sacrificial reagent of $\text{O}_2^{\bullet-}$ (BQ) was added to the CN and 50PCN photocatalytic systems (Fig. S17). These results confirmed that the CN and 50PCN underwent a sequential two-step single-electron O_2 reduction route for H_2O_2 generation. In other words, $\text{O}_2^{\bullet-}$ was first formed by single electron reduction of O_2 , and then H_2O_2 was generated from $\text{O}_2^{\bullet-}$ through the proton coupled electron transfer (PCET) process.

DFT calculations were carried out to explore the mechanism of O_2 reduction to H_2O_2 over CN, PCN_corner, and PCN_bay. The reduction reaction consisted of three elementary steps, (i) O_2 molecules can be adsorbed on catalyst to form $^*\text{O}_2$, (ii) $^*\text{O}_2$ coupled a proton-electron pair to generate $^*\text{OOH}$, (iii) $^*\text{OOH}$ species captured another proton-electron pair to produce $^*\text{H}_2\text{O}_2$. As shown in Fig. 5e, f, the relatively low adsorption energy (-0.112 eV) and long adsorption distance (about 3.3 Å) of generating $^*\text{O}_2$ on CN implied the physical adsorption on the

Table 1
 D_{index} , $S_{r,\text{index}}$, and t_{index} of the CN and PCN.

	Excitation type	D_{index} (Å)	$S_{r,\text{index}}$ (a.u)	t (Å)
CN	$S_0 \rightarrow S_3$ (LE)	0.35	0.55	-3.75
PCN_corner	$S_0 \rightarrow S_4$ (CT)	5.42	0.14	3.52
PCN_bay	$S_0 \rightarrow S_3$ (CT)	5.56	0.09	4.01

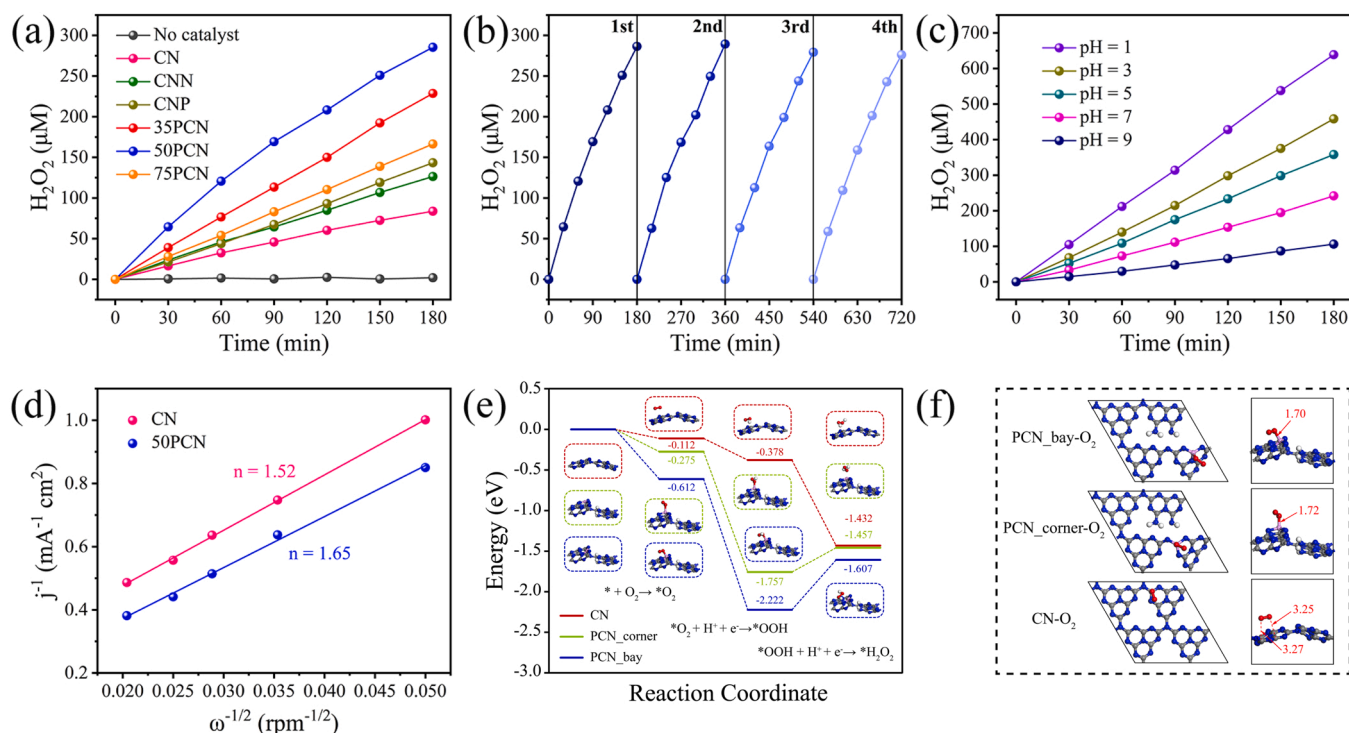


Fig. 5. (a) The photocatalytic H₂O₂ production over different catalysts under blue LED light irradiation. (b) Reusability of 50PCN for the photocatalytic H₂O₂ production with four times of cycling uses. (c) The photocatalytic H₂O₂ production over 50PCN at different initial pH values. (d) The Koutecky-Levich plots of the data obtained by RDE measurements in an O₂-saturated 0.5 M H₂SO₄ solution at -1.0 V (vs Ag/AgCl). (e) Gibbs free energy diagrams for O₂ reduction to H₂O₂ over CN, PCN_bay, and PCN_corner. (f) Optimized structures and key parameters of CN-O₂, PCN_bay-O₂ and PCN_corner-O₂.

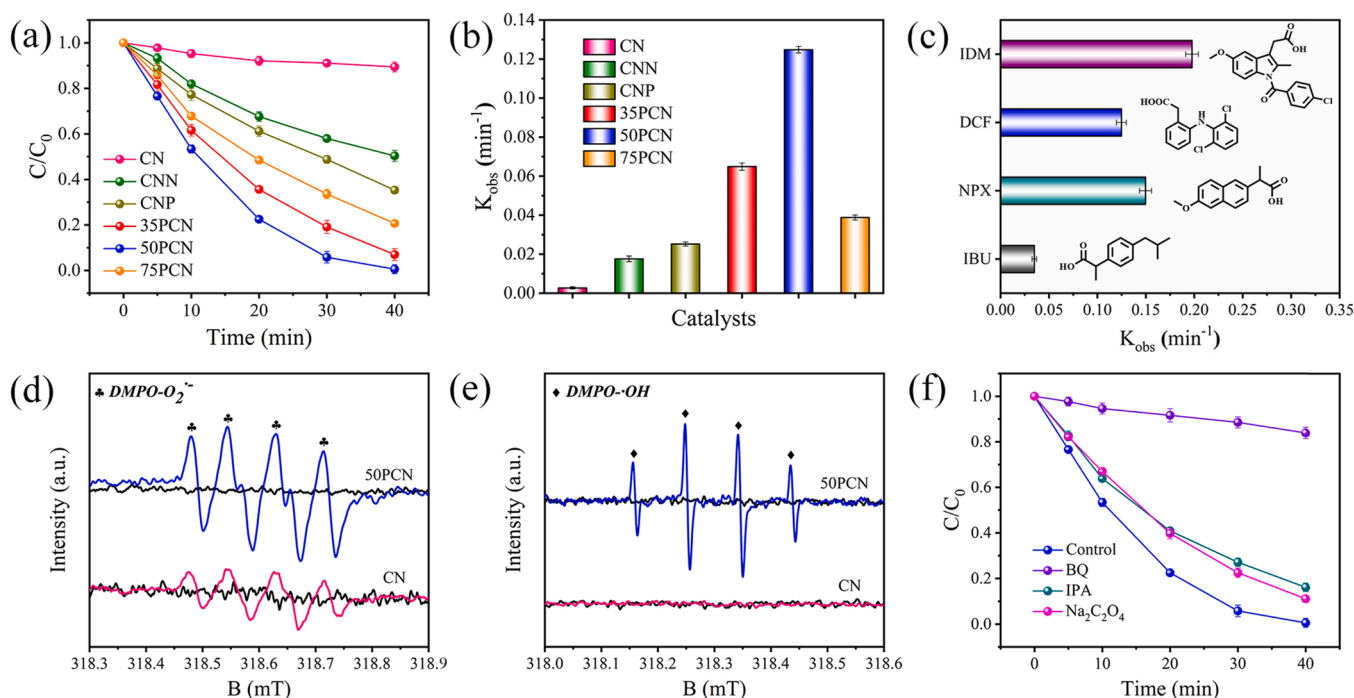


Fig. 6. (a) Photocatalytic activity of the samples based on the photocatalytic degradation of DCF (b) Kinetic rate constants of DCF degradation over different photocatalysts. (c) Kinetic rate constants of NSAIDs over the 50PCN photocatalyst. ESR spectra of the (d) DMPO-O₂^{•-} adducts, (e) DMPO-•OH adducts, recorded with the CN and 50PCN under dark and light irradiation. (f) Photocatalytic degradation of DCF over the 50PCN photocatalytic system with different scavengers.

catalyst. Conversely, adsorption of O₂ on PCN_bay, and PCN_corner was chemical adsorption for the relative high adsorption energy (-0.612 and -0.275 eV) and short adsorption distance (1.70 and 1.72 Å). Therefore, P doping was beneficial to the adsorption of O₂ on the catalyst, which

was also demonstrated by our O₂-TPD experiments (Fig. S14). And then, the more stable adsorption of O₂ on PCNs enhanced the following generation of H₂O₂.

3.5. Photocatalytic degradation of NSAIDs

3.5.1. Photocatalytic degradation performance and mechanism

Fig. S18 reveals that all samples achieved DCF adsorption-desorption equilibrium after 30 min in a dark adsorption experiment. The CN had a negligible adsorption capacity for the DCF, while the 50PCN adsorbed 21.3% of the DCF, which was consistent with the BET results. The photocatalytic activities of all the samples were evaluated through the degradation of DCF under blue LED light irradiation. As shown in Fig. 6a, the CN exhibited very weak photocatalytic activity for the degradation of DCF. Only 10.6% of the DCF was removed within 40 min of reaction time, while the CNN degraded 49.7% of the DCF. This may have been attributed to the porous structure of the CNN, which expanded the specific surface area and provided a higher population of reaction sites. It can be seen that the P-doped samples further improved the degradation of DCF. Among them, the 50PCN exhibited the best DCF removal efficiency of 99.4%. Notably, further increase of the P doping resulted in a decreased degradation efficiency of DCF due to that excessive doping inhibited the separation of photogenerated carriers. Furthermore, the photodegradation kinetics of DCF by all photocatalysts were also investigated (Fig. 6b). The degradation rate constants of the CN, CNN, CNP, 35PCN, 50PCN, and 75PCN were 0.0027, 0.0176, 0.0252, 0.0649, 0.1248, and 0.0388 min⁻¹, respectively. The 50PCN exhibited the best degradation rate constant, which was 46.22 times that of the CN.

Since the optical properties of the aqueous photocatalysts suspensions played a crucial role in the photocatalytic reactions, the optical properties of the CN and 50PCN were determined to better compare their photocatalytic performance [34,51]. The absorption spectra of the CN and 50PCN aqueous suspensions with different concentrations were measured by UV-vis spectrophotometry (Fig. S19). Subsequently, the UV-vis diffuse reflectance spectra of the CN and 50PCN solids were also determined (Fig. S20). Based on the Kubelka-Munk method, the specific extinction coefficient β_{λ}^* , absorption coefficient κ_{λ}^* , and scattering coefficient σ_{λ}^* were estimated by combining the above data (Fig. S21). The spectral-averaged absorption and scattering coefficients κ^* and σ^* of the CN aqueous suspension were calculated to be 403.6 cm² g⁻¹ and 1964.0 cm² g⁻¹, while the κ^* and σ^* of the PCN aqueous suspension were 1427.6 cm² g⁻¹ and 1681.4 cm² g⁻¹. Considering the configuration of our photocatalytic reactor (Fig. S1), δ was equal to the depth of the suspension and was measured to be 2.7 cm. Thus, the optical thickness of the CN and 50PCN aqueous suspensions in this system were calculated to be 2.6 and 3.4, respectively, which were close to the reported optimum optical thickness (2–3) for photocatalytic reactors [35]. In addition, we conducted experiments under the same optical thickness ($\tau = 3$) to compare the photocatalytic performance of the CN and 50PCN. As shown in Fig. S22, both the CN and 50PCN exhibited a slight increase degradation efficiency of DCF, but the performance of the 50PCN was still much better than that of the CN.

A number of typical non-steroidal anti-inflammatory drugs (NSAIDs) were employed to evaluate the photocatalytic performance of the 50PCN. Fig. 6c depicts the degradation rate constants for indomethacin (IDM), diclofenac (DCF), naproxen (NPX), and ibuprofen (IBU) degradation using the 50PCN/blue-LED system, with rate constants of 0.1977, 0.1248, 0.1497, and 0.0349 min⁻¹, respectively. These results suggested that the 50PCN could photodegrade all four NSAIDs. The removal rate varied with the type of NSAIDs, which may have been related to their molecular structure, physicochemical properties, and the adsorption capacity of the 50PCN.

The stability of the 50PCN photocatalyst was investigated via cyclic photocatalytic DCF degradation experiments under the same conditions. As shown in Fig. S23a, the 50PCN maintained a high degradation efficiency for DCF without significant reduction after four cycles. Moreover, the TEM images, XRD patterns, and FT-IR spectra (Figs. S23b-d) also verified that the morphology and chemical structure of the 50PCN changed only negligibly following four photocatalytic reactions, which

confirmed that the 50PCN exhibited excellent stability and reusability. Generally, oxygen was essential for the photocatalytic degradation process. Fig. S24 shows the photocatalytic degradation rate of DCF by the 50PCN under continuous bubbling O₂ or N₂ conditions. Under an O₂ atmosphere, the DCF was almost totally degraded within 20 min, which indicated that the photocatalytic performance of 50PCN was remarkably enhanced. However, a sharp decline in the photocatalytic activity was observed under a N₂ atmosphere.

Reactive oxygen species (ROSs) generated in the 50PCN photocatalytic system were detected by the ESR technique using DMPO as the spin-trapping agent. As illustrated in Fig. 6d, e, no ESR signals were detected under dark conditions, while the ESR signals of DMPO-O₂^{•-} and DMPO-•OH adducts could be observed under light irradiation, which indicated the generation of O₂^{•-} and •OH in the photocatalytic system. Interestingly, no DMPO-•OH signals could be recorded in the CN photocatalytic system. Further, compared with the CN, both the DMPO-O₂^{•-} and DMPO-•OH signals of the 50PCN were significantly stronger, which suggested that more ROSs could be generated following the creation of the porous structure and doping with phosphorus atoms.

Quenching experiments were performed with the CN and 50PCN photocatalytic systems to further clarify the role of specific reaction species for DCF degradation. The addition of BQ, Na₂C₂O₄, and IPA was used to investigate the effect of formed O₂^{•-}, h⁺, and •OH on the DCF degradation, respectively. As shown in Fig. 6f and S25, when BQ was added into the CN and 50PCN photocatalytic systems, the degradation efficiency of DCF was most inhibited compared with other quenchers, which indicated that O₂^{•-} was the dominant active species on the CN and 50PCN. In the presence of Na₂C₂O₄, the degradation efficiency of DCF in the 50PCN system slightly decreased, while that in the CN system slightly increased. It was worth noting that the addition of IPA effectively inhibited the DCF degradation in the 50PCN system, but had no obvious effect on the DCF degradation in the CN system, which was consistent with the ESR results. In addition, we explored the production of H₂O₂ during the degradation of DCF by the 50PCN. It can be seen from Fig. S26 that the degradation process of DCF was conducive to the production of H₂O₂, which may have been attributed to the fact that organic pollutants can act as electron donors to accelerate the reduction half-reaction [52]. Therefore, it was expected that the 50PCN would be developed as a dual-function photocatalytic system for the oxidation of organic pollutants and the production of H₂O₂.

Based on the above results and discussion, the photocatalytic mechanism of the 50PCN photocatalyst was proposed as illustrated in Fig. 7. Under blue LED light irradiation, the photogenerated electron-hole pairs were generated on 50PCN. Since the conduction band (CB) position of the 50PCN (-0.52 V vs. NHE, Fig. S27) was more negative than the standard reduction potential of O₂/O₂^{•-} (-0.33 V vs. NHE), the photogenerated electrons on the CB easily reacted with molecular oxygen to generate O₂^{•-}. However, the valence band (VB) position of 50PCN (+1.68 V vs. NHE) was much lower than the standard oxidation potential of OH⁻/•OH (+1.99 V vs. NHE), and the photogenerated holes could not oxidize OH⁻ or H₂O to generate •OH. Fortunately, with the creation of the porous structure and P atoms, the 50PCN exhibited enhanced O₂ adsorption, promoted O₂ reduction reaction, and the rapid separation of photogenerated electrons and holes, thereby generating more •OH. Subsequently, the h⁺, O₂^{•-}, and •OH attacked the NSAIDs molecules, which resulted in their decomposition and mineralization (Eqs. 9–15). For the CN, its photocatalytic mechanism was similar to that of the 50PCN, but the role of •OH in the photocatalytic mechanism was negligible.



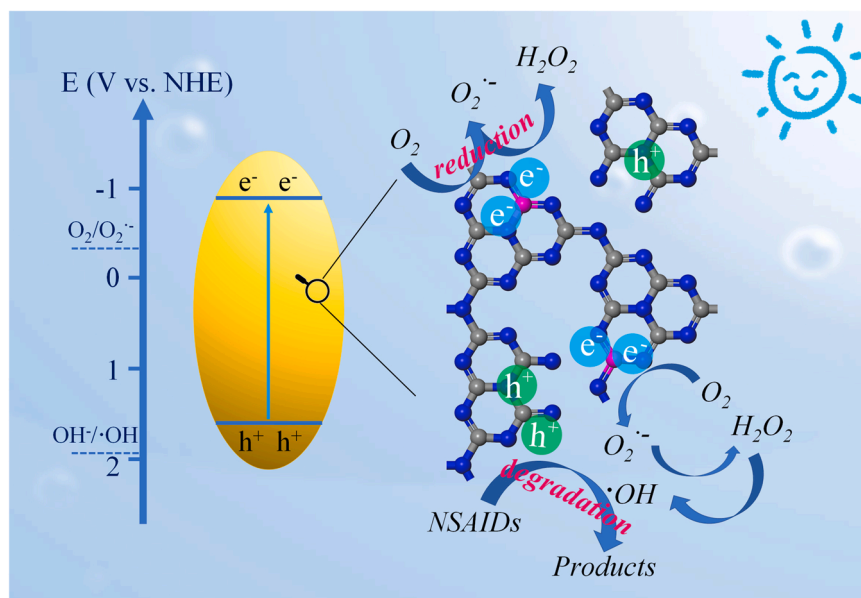


Fig. 7. Proposed photocatalytic mechanism in the 50PCN system under blue LED light irradiation.



3.5.2. Effects of environmental factors and transformation pathways

The effects of the catalyst dosage were closely related to the optical thickness of the suspension and the volume rate of photon absorption (VRPA) [36,53]. As shown in Fig. 8a, as the added amounts of the 50PCN

photocatalyst increased from 0.1 g L⁻¹ to 0.4 g L⁻¹, the degradation efficiency of DCF gradually increased, which was attributed to sufficient photon absorption, additional active sites and free radicals. However, when the quantity of added 50PCN was increased to 0.8 g L⁻¹, the photocatalytic efficiency slightly decreased due to the increase of the photon shielding effects. The photon scattering and shielding effects were related to the optical thickness of the suspension. The optical thickness at the lower photocatalyst concentration (0.1 g L⁻¹) was 0.8, while at the higher catalyst concentrations (0.8 g L⁻¹) it was 6.7. These values were far from the optimal range, which indicated that the photon absorption efficiency would be reduced, resulting in lower degradation efficiency of DCF [53].

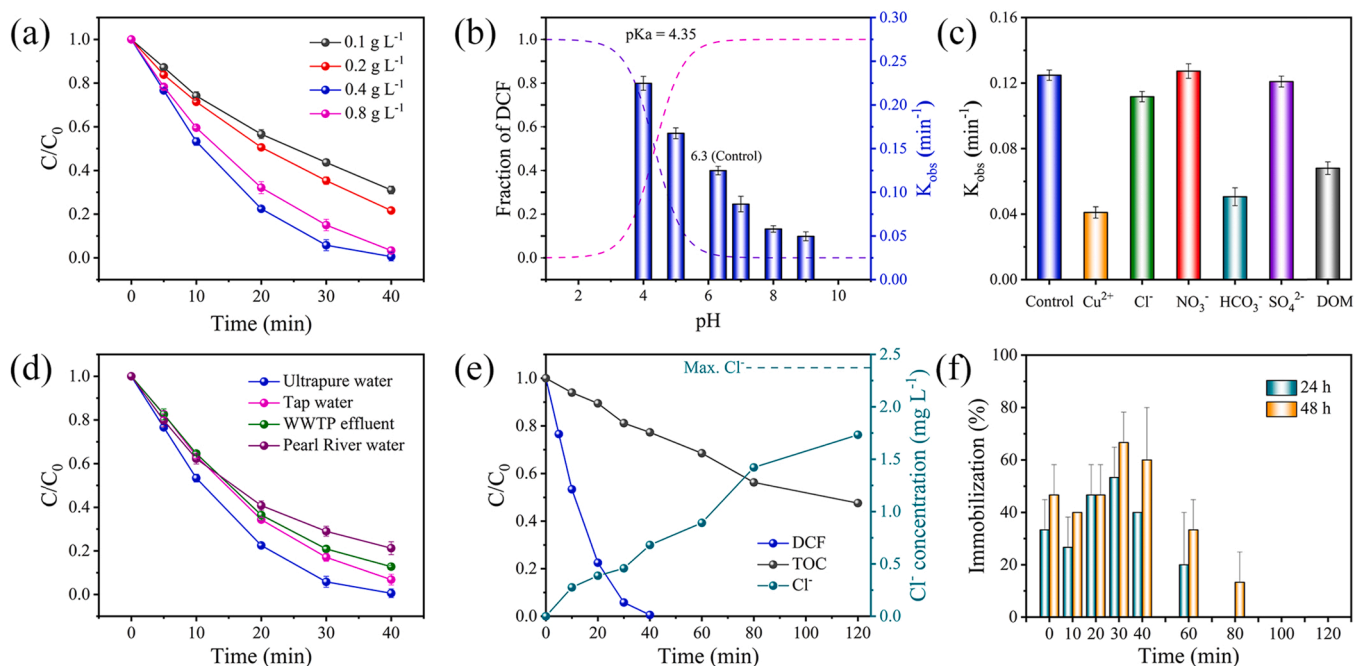


Fig. 8. (a) Effects of 50PCN dosage on photocatalytic degradation of DCF. (b) Effects of initial pH values on kinetic rate constants for degradation of DCF ($[\text{Cu}^{2+}] = 5 \text{ mg L}^{-1}$; concentrations of all other water quality constituents were 10 mg L^{-1}). (c) Effects of water quality constituents on kinetic rate constants for degradation of DCF. (d) Photocatalytic degradation of DCF in different water and wastewater matrices. (e) TOC removal and generation of chloride during the degradation of DCF by the 50PCN. (f) Acute toxicity evaluated with *Daphnia magna* for 24 h and 48 h.

In addition, the effects of initial pH values on the degradation performance of DCF over the 50PCN was investigated as presented in Fig. 8b. The degradation rate constant for DCF was drastically reduced, from 0.2247 min^{-1} at pH = 4.0 to 0.0496 min^{-1} at pH = 9, which suggested that the degradation efficiency of DCF by the 50PCN was inhibited at higher pH values. The dissociation constant (pK_a) of DCF was 4.35 [54], and the zero potential of the 50PCN was measured to be 3.70 (Fig. S28). When the pH value of the reaction system was from between 3.70 and 4.35, electrostatic attraction may have occurred between the 50PCN and protonated DCF, which was beneficial for improving the photocatalytic activity. However, when pH value exceeded 4.35, electrostatic repulsion occurred between the 50PCN and deprotonated DCF, which resulted in the decrease of photocatalytic activity.

Anions, cations, and dissolved organic matter (DOM) are critical parameters in aqueous ecosystems; thus, their influence on the photodegradation of DCF was investigated (Fig. 8c). In the presence of Cl^- , NO_3^- , and SO_4^{2-} , the degradation rate constant of DCF was not obviously affected; however, it was significantly inhibited with the addition of HCO_3^- . This inhibitory effect may have been attributed to the capacity of HCO_3^- to scavenge $\bullet\text{OH}$ [55]. Moreover, as an electron scavenger, Cu^{2+} showed the highest inhibition for the degradation of DCF. The addition of DOM also inhibited the photocatalytic degradation of DCF, which was likely due to competing reactions between reactive species and light-screening effects [56].

Furthermore, the photocatalytic performance of the 50PCN in diverse water matrices was also explored. As illustrated in Fig. 8d, the 50PCN exhibited the highest DCF removal rate in ultrapure water. The degradation of DCF by the 50PCN photocatalyst in tap water, WWTP effluent, and Pearl River water was reduced by varying degrees, which may have been attributed to active species scavenging and light shielding by ions and DOM in these water matrices. Notably, the removal rates of DCF in tap water, WWTP effluent, and Pearl River water were 93.2%, 87.6%, and 78.8%, respectively, which indicated the applicability of the 50PCN system for water in the ambient environment and potable water.

Fig. 8e reveals the degree of DCF mineralization in the 50PCN photocatalytic system. Following 40 min of treatment, the DCF mineralization rate and dechlorination rate were only 22.7% and 28.5%, respectively. However, as the treatment time was extended to 120 min, the DCF mineralization rate attained 52.4%, and the dechlorination rate approached 72.4%. Furthermore, according to OECD guidelines [57], an acute toxicity of *Daphnia magna* (48 h) was conducted to evaluate the potential ecological risks of transformation products during the DCF photodegradation. As shown in Fig. 8f, when the treatment time increased, the immobilization rate of *Daphnia magna* gradually decreased, which meant that the toxicity of the test solution was

reduced. The increased immobilization rate at 30 min may have been due to the generation of additional toxic by-products during the DCF photodegradation. These results confirmed that the 50PCN photocatalytic system exhibited excellent performance for DCF mineralization and detoxification.

There was no doubt that a series of transformation products were produced during the degradation of DCF. To explore the pathways of DCF degradation via the 50PCN photocatalytic system, UPLC-Q-TOF MS analysis was performed on the reaction solution. The detailed information of the 15 potential intermediate products and their MS/MS results are provided in Table S6. Ultimately, three degradation pathways of DCF were proposed (Fig. 9).

Pathway I was the decarboxylation reaction. According to our previous research [58], the C8 position of the DCF molecule displayed a higher positive charge and was susceptible to $\text{O}_2^{\bullet-}$ attack, which resulted in the release of a carboxylate group and the formation of P1. The P1 suffered from the loss of chlorine and hydrogen atoms, which led to ring closure and formation of P2. The generation of P3 was likely due to the $\bullet\text{OH}$ attack at the chlorine position, which replaced a chlorine atom with an OH group [59].

Pathway II was the ketone formation reaction. Generally speaking, sites with higher electron cloud densities were more vulnerable to the $\bullet\text{OH}$ electrophilic reaction [55]. Consequently, $\bullet\text{OH}$ was expected to attack the C2 and C16 positions, which resulted in the generation of P4 and P8 intermediates [60]. On one hand, P4 may have undergone a dehydrogenation reaction (-2H) to generate P5, which was further attacked by h^+ and decarboxylated to form P7 [61]. On the other hand, P4 underwent cyclization with the loss of water to form P6, which was then further oxidized to P7 by active species, as previously reported [62, 63]. In another reaction, ROSs attacked the N12 site on P8 through C-N cleavage to generate P9 and P10.

Pathway III was the aldehyde reaction. Due to its nucleophilic properties, $\text{O}_2^{\bullet-}$ was suggested to preferentially attack the C17 position on DCF with a low charge density to form a zwitterion or a diradical [58]. However, the intermediate structure was unstable, particularly in water, which would collapse to produce aldehydes to produce P11, which was further hydrolyzed to form aldehyde carboxylic acid (P12) [64]. Furthermore, the transformation products identified from the three pathways might undergo C-N cleavage and ring-opening reactions, resulting in their degradation to small molecular compounds (e.g., P13, P14, and P15), and eventually mineralize to CO_2 and H_2O .

4. Conclusion

In summary, an ultrathin porous phosphorus-doped $\text{g-C}_3\text{N}_4$ nano-sheet was successfully prepared by a simple one-step thermal polymerization method, which exhibited excellent photocatalytic performance

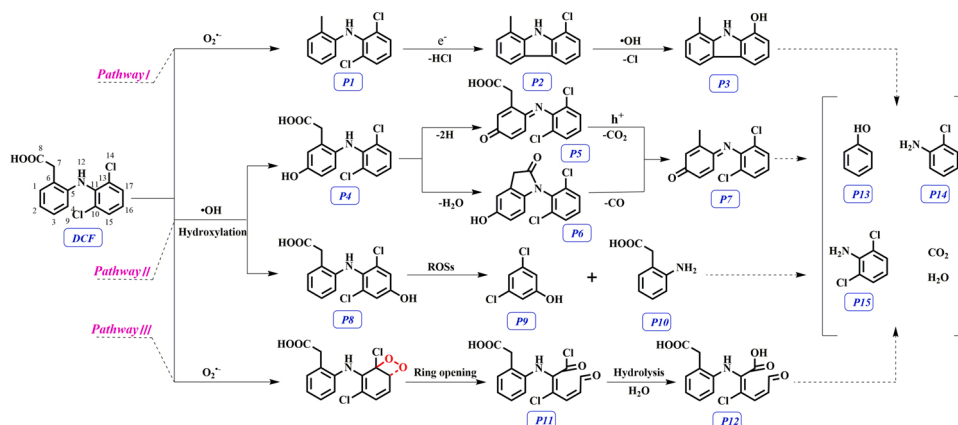


Fig. 9. Proposed transformation pathways of DCF during the 50PCN photocatalytic degradation process under blue LED light irradiation.

for the production of H_2O_2 and degradation of NSAIDs under blue LED light irradiation. The production of H_2O_2 by 50PCN reached $285.34 \mu\text{M}$ within 3 h, which was 3.41 times that of the CN. Moreover, the rate constant for DCF degradation by the 50PCN was 46.22 times that of the CN. Importantly, DFT calculations revealed that P doping regulated the electronic structure of the CN. The recombination of electrons and holes in 50PCN was more difficult than in CN. Due to the low electronic localization and small work function of P-doped sites, electrons were easily transferred to small molecular substances, thereby improving the separation and transfer of photogenerated carriers. RDE measurements further demonstrated that the 50PCN generated H_2O_2 through sequential two-step single-electron O_2 reduction reactions. In addition, ESR and quenching experiments verified that $\text{O}_2^{\bullet-}$ and $\bullet\text{OH}$ were the major reactive species in the 50PCN photocatalytic degradation process, after which a detailed photocatalytic mechanism was proposed. The 50PCN possessed outstanding stability and good applicability in actual ambient water. The DCF degradation pathways primarily included the decarboxylation reaction, ketone formation reaction, and aldehyde reaction. This work provides an attractive two-in-one strategy for addressing energy demands and environmental remediation issues.

CRedit authorship contribution statement

Daguang Li: Conceptualization, Investigation, Validation, Formal analysis, Writing – original draft, Writing – review & editing. **Chenghui Wen:** Investigation, Validation, Writing – review & editing. **Jiaxing Huang:** Validation, Supervision. **Jiapeng Zhong:** Investigation. **Ping Chen:** Supervision, Funding acquisition. **Haijin Liu:** Writing – review & editing. **Zhongquan Wang:** Resources. **Yang Liu:** Methodology, Formal analysis, Software, Resources. **Wenyang Lv:** Funding acquisition. **Guoguang Liu:** Conceptualization, Resources, Project administration, Funding acquisition.

Declaration of Competing Interest

The authors declare that they have no known competing financial interests or personal relationships that could have appeared to influence the work reported in this paper.

Acknowledgements

This work was supported by the National Natural Science Foundation of China (21677040, 22076029 and 21906029), and the Guangzhou Municipal Science and Technology Project (201903010080).

Appendix A. Supporting information

Supplementary data associated with this article can be found in the online version at [doi:10.1016/j.apcatb.2022.121099](https://doi.org/10.1016/j.apcatb.2022.121099).

References

- T. Wu, X. Liu, Y. Liu, M. Cheng, Z. Liu, G. Zeng, B. Shao, Q. Liang, W. Zhang, Q. He, W. Zhang, Application of QD-MOF composites for photocatalysis: energy production and environmental remediation, *Coord. Chem. Rev.* 403 (2020), 213097.
- J.C. López-Doval, A. Serra-Compte, S. Rodríguez-Mozaz, D. Barceló, S. Sabater, Diet quality and NSAIDs promote changes in formation of prostaglandins by an aquatic invertebrate, *Chemosphere* 257 (2020), 126892.
- T. Aus Der Beek, F.-A. Weber, A. Bergmann, S. Hickmann, I. Ebert, A. Hein, A. Küster, Pharmaceuticals in the environment—global occurrences and perspectives, *Environ. Toxicol. Chem.* 35 (2016) 823–835.
- P. Chen, Q. Zhang, L. Shen, R. Li, C. Tan, T. Chen, H. Liu, Y. Liu, Z. Cai, G. Liu, W. Lv, Insights into the synergetic mechanism of a combined vis-RGO/TiO₂/peroxodisulfate system for the degradation of PPCPs: kinetics, environmental factors and products, *Chemosphere* 216 (2019) 341–351.
- M. Parolini, Toxicity of the non-steroidal anti-inflammatory drugs (NSAIDs) acetylsalicylic acid, paracetamol, diclofenac, ibuprofen and naproxen towards freshwater invertebrates: a review, *Sci. Total Environ.* 740 (2020), 140043.
- Z. Lu, W. Sun, C. Li, X. Ao, C. Yang, S. Li, Bioremoval of non-steroidal anti-inflammatory drugs by *Pseudoxanthomonas* sp. DIN-3 isolated from biological activated carbon process, *Water Res.* 161 (2019) 459–472.
- K. Mase, M. Yoneda, Y. Yamada, S. Fukuzumi, Seawater usable for production and consumption of hydrogen peroxide as a solar fuel, *Nat. Commun.* 7 (2016) 11470.
- S.A. Mousavi Shaegh, N.-T. Nguyen, S.M. Mousavi Ehteshami, S.H. Chan, A membraneless hydrogen peroxide fuel cell using prussian blue as cathode material, *Energy Environ. Sci.* 5 (2012) 8225–8228.
- S.O. Ganiyu, M. Zhou, C.A. Martínez-Huitle, Heterogeneous electro-Fenton and photoelectro-Fenton processes: a critical review of fundamental principles and application for water/wastewater treatment, *Appl. Catal. B Environ.* 235 (2018) 103–129.
- X.-j. Yang, X.-m. Xu, J. Xu, Y.-f. Han, Iron oxychloride (FeOCl): an efficient Fenton-like catalyst for producing hydroxyl radicals in degradation of organic contaminants, *J. Am. Chem. Soc.* 135 (2013) 16058–16061.
- A.L.-T. Pham, C. Lee, F.M. Doyle, D.L. Sedlak, A silica-supported iron oxide catalyst capable of activating hydrogen peroxide at neutral pH values, *Environ. Sci. Technol.* 43 (2009) 8930–8935.
- J.M. Campos-Martin, G. Blanco-Brieva, J.L.G. Fierro, Hydrogen peroxide synthesis: an outlook beyond the anthraquinone process, *Angew. Chem. Int. Ed.* 45 (2006) 6962–6984.
- T.-j. Fellingner, F. Hasché, P. Strasser, M. Antonietti, Mesoporous nitrogen-doped carbon for the electrocatalytic synthesis of hydrogen peroxide, *J. Am. Chem. Soc.* 134 (2012) 4072–4075.
- D.W. Flaherty, Direct synthesis of H_2O_2 from H_2 and O_2 on Pd catalysts: current understanding, outstanding questions, and research needs, *ACS Catal.* 8 (2018) 1520–1527.
- Z. Wei, M. Liu, Z. Zhang, W. Yao, H. Tan, Y. Zhu, Efficient visible-light-driven selective oxygen reduction to hydrogen peroxide by oxygen-enriched graphitic carbon nitride polymers, *Energy Environ. Sci.* 11 (2018) 2581–2589.
- Z. Zheng, Y.H. Ng, D.-W. Wang, R. Amal, Epitaxial growth of Au–Pt–Ni nanorods for direct high selectivity H_2O_2 production, *Adv. Mater.* 28 (2016) 9949–9955.
- G. Mamba, A.K. Mishra, Graphitic carbon nitride (g-C₃N₄) nanocomposites: a new and exciting generation of visible light driven photocatalysts for environmental pollution remediation, *Appl. Catal. B-Environ.* 198 (2016) 347–377.
- L. Zhou, J. Feng, B. Qiu, Y. Zhou, J. Lei, M. Xing, L. Wang, Y. Zhou, Y. Liu, J. Zhang, Ultrathin g-C₃N₄ nanosheet with hierarchical pores and desirable energy band for highly efficient H_2O_2 production, *Appl. Catal. B-Environ.* 267 (2020), 118396.
- X. Zeng, Y. Liu, Y. Kang, Q. Li, Y. Xia, Y. Zhu, H. Hou, M.H. Uddin, T. R. Gengenbach, D. Xia, C. Sun, D.T. McCarthy, A. Deletic, J. Yu, X. Zhang, Simultaneously tuning charge separation and oxygen reduction pathway on graphitic carbon nitride by polyethylenimine for boosted photocatalytic hydrogen peroxide production, *ACS Catal.* 10 (2020) 3697–3706.
- S. Li, G. Dong, R. Hailili, L. Yang, Y. Li, F. Wang, Y. Zeng, C. Wang, Effective photocatalytic H_2O_2 production under visible light irradiation at g-C₃N₄ modulated by carbon vacancies, *Appl. Catal. B Environ.* 190 (2016) 26–35.
- Y. Wang, B. Jing, F. Wang, S. Wang, X. Liu, Z. Ao, C. Li, Mechanism Insight into enhanced photodegradation of pharmaceuticals and personal care products in natural water matrix over crystalline graphitic carbon nitrides, *Water Res.* 180 (2020), 115925.
- G. Zhang, G. Li, Z.-A. Lan, L. Lin, A. Savateev, T. Heil, S. Zafeirotas, X. Wang, M. Antonietti, Optimizing optical absorption, exciton dissociation, and charge transfer of a polymeric carbon nitride with ultrahigh solar hydrogen production activity, *Angew. Chem. Int. Ed.* 56 (2017) 13445–13449.
- J. Chen, C.-L. Dong, D. Zhao, Y.-C. Huang, X. Wang, L. Samad, L. Dang, M. Shearer, S. Shen, L. Guo, Molecular design of polymer heterojunctions for efficient solar-hydrogen conversion, *Adv. Mater.* 29 (2017) 1606198.
- P. Niu, L. Zhang, G. Liu, H.-M. Cheng, Graphene-like carbon nitride nanosheets for improved photocatalytic activities, *Adv. Funct. Mater.* 22 (2012) 4763–4770.
- W. Iqbal, C. Dong, M. Xing, X. Tan, J. Zhang, Eco-friendly one-pot synthesis of well-adorned mesoporous g-C₃N₄ with efficiently enhanced visible light photocatalytic activity, *Catal. Sci. Technol.* 7 (2017) 1726–1734.
- D. Li, J. Huang, R. Li, P. Chen, D. Chen, M. Cai, H. Liu, Y. Feng, W. Lv, G. Liu, Synthesis of a carbon dots modified g-C₃N₄/SnO₂ Z-scheme photocatalyst with superior photocatalytic activity for PPCPs degradation under visible light irradiation, *J. Hazard. Mater.* 401 (2021), 123257.
- S. Yang, Y. Gong, J. Zhang, L. Zhan, L. Ma, Z. Fang, R. Vajtai, X. Wang, P. M. Ajayan, Exfoliated graphitic carbon nitride nanosheets as efficient catalysts for hydrogen evolution under visible light, *Adv. Mater.* 25 (2013) 2452–2456.
- Y. Li, R. Jin, Y. Xing, J. Li, S. Song, X. Liu, M. Li, R. Jin, Macroscopic foam-like holey ultrathin g-C₃N₄ nanosheets for drastic improvement of visible-light photocatalytic activity, *Adv. Energy Mater.* 6 (2016) 1601273.
- S. Liu, H. Zhu, W. Yao, K. Chen, D. Chen, One step synthesis of P-doped g-C₃N₄ with the enhanced visible light photocatalytic activity, *Appl. Surf. Sci.* 430 (2018) 309–315.
- Y. Zhang, T. Mori, J. Ye, M. Antonietti, Phosphorus-doped carbon nitride solid: enhanced electrical conductivity and photocurrent generation, *J. Am. Chem. Soc.* 132 (2010) 6294–6295.
- J. Ran, T.Y. Ma, G. Gao, X.-W. Du, S.Z. Qiao, Porous P-doped graphitic carbon nitride nanosheets for synergistically enhanced visible-light photocatalytic H_2 production, *Energy Environ. Sci.* 8 (2015) 3708–3717.
- Y. Deng, L. Tang, G. Zeng, Z. Zhu, M. Yan, Y. Zhou, J. Wang, Y. Liu, J. Wang, Insight into highly efficient simultaneous photocatalytic removal of Cr(VI) and 2,4-dichlorophenol under visible light irradiation by phosphorus doped porous ultrathin g-C₃N₄ nanosheets from aqueous media: performance and reaction mechanism, *Appl. Catal. B Environ.* 203 (2017) 343–354.

- [33] A.E. Cassano, O.M. Alfano, Reaction engineering of suspended solid heterogeneous photocatalytic reactors, *Catal. Today* 58 (2000) 167–197.
- [34] I. Grčić, G. Li Puma, Six-flux absorption-scattering models for photocatalysis under wide-spectrum irradiation sources in annular and flat reactors using catalysts with different optical properties, *Appl. Catal. B Environ.* 211 (2017) 222–234.
- [35] Q. Liao, D. Wang, C. Ke, Y. Zhang, Q. Han, Y. Zhang, K. Xi, Metal-free Fenton-like photocatalysts based on covalent organic frameworks, *Appl. Catal. B Environ.* 298 (2021), 120548.
- [36] R. Acosta-Herazo, M.Á. Mueses, G.L. Puma, F. Machuca-Martínez, Impact of photocatalyst optical properties on the efficiency of solar photocatalytic reactors rationalized by the concepts of initial rate of photon absorption (IRPA) dimensionless boundary layer of photon absorption and apparent optical thickness, *Chem. Eng. J.* 356 (2019) 839–849.
- [37] C. Kormann, D.W. Bahnemann, M.R. Hoffmann, Photocatalytic production of hydrogen peroxides and organic peroxides in aqueous suspensions of titanium dioxide, zinc oxide, and desert sand, *Environ. Sci. Technol.* 22 (1988) 798–806.
- [38] X. Wang, K. Maeda, A. Thomas, K. Takanabe, G. Xin, J.M. Carlsson, K. Domen, M. Antonietti, A metal-free polymeric photocatalyst for hydrogen production from water under visible light, *Nat. Mater.* 8 (2009) 76–80.
- [39] Y. Kang, Y. Yang, L.-C. Yin, X. Kang, G. Liu, H.-M. Cheng, An amorphous carbon nitride photocatalyst with greatly extended visible-light-responsive range for photocatalytic hydrogen generation, *Adv. Mater.* 27 (2015) 4572–4577.
- [40] S. Cao, B. Fan, Y. Feng, H. Chen, F. Jiang, X. Wang, Sulfur-doped g-C₃N₄ nanosheets with carbon vacancies: general synthesis and improved activity for simulated solar-light photocatalytic nitrogen fixation, *Chem. Eng. J.* 353 (2018) 147–156.
- [41] B. Jürgens, E. Irran, J. Senker, P. Kroll, H. Müller, W. Schnick, Melem (2,5,8-triamino-tri-s-triazine), an important intermediate during condensation of melamine rings to graphitic carbon nitride: synthesis, structure determination by X-ray powder diffractometry, solid-state NMR, and theoretical studies, *J. Am. Chem. Soc.* 125 (2003) 10288–10300.
- [42] S. Guo, Y. Tang, Y. Xie, C. Tian, Q. Feng, W. Zhou, B. Jiang, P-doped tubular g-C₃N₄ with surface carbon defects: universal synthesis and enhanced visible-light photocatalytic hydrogen production, *Appl. Catal. B Environ.* 218 (2017) 664–671.
- [43] J. Zhang, G. Zhang, X. Chen, S. Lin, L. Möhlmann, G. Dolgga, G. Lipner, M. Antonietti, S. Blechert, X. Wang, Co-monomer control of carbon nitride semiconductors to optimize hydrogen evolution with visible light, *Angew. Chem. Int. Ed.* 51 (2012) 3183–3187.
- [44] F. Wang, T. Hou, X. Zhao, W. Yao, R. Fang, K. Shen, Y. Li, Ordered macroporous carbonous frameworks implanted with CdS quantum dots for efficient photocatalytic CO₂ reduction, *Adv. Mater.* 33 (2021) 2102690.
- [45] Z. Zhang, Y. Huang, K. Liu, L. Guo, Q. Yuan, B. Dong, Multichannel-improved charge-carrier dynamics in well-designed hetero-nanostructural plasmonic photocatalysts toward highly efficient solar-to-fuels conversion, *Adv. Mater.* 27 (2015) 5906–5914.
- [46] M.-Q. Yang, Y.-J. Xu, W. Lu, K. Zeng, H. Zhu, Q.-H. Xu, G.W. Ho, Self-surface charge exfoliation and electrostatically coordinated 2D hetero-layered hybrids, *Nat. Commun.* 8 (2017) 14224.
- [47] S. Wang, B.Y. Guan, X.W.D. Lou, Construction of ZnIn₂S₄-In₂O₃ hierarchical tubular heterostructures for efficient CO₂ photoreduction, *J. Am. Chem. Soc.* 140 (2018) 5037–5040.
- [48] F. Wang, G. Qian, X.-P. Kong, X. Zhao, T. Hou, L. Chen, R. Fang, Y. Li, Hierarchical double-shelled CoP nanocages for efficient visible-light-driven CO₂ reduction, *ACS Appl. Mater. Interfaces* 13 (2021) 45609–45618.
- [49] Y. Shiraishi, S. Kanazawa, Y. Sugano, D. Tsukamoto, H. Sakamoto, S. Ichikawa, T. Hirai, Highly selective production of hydrogen peroxide on graphitic carbon nitride (g-C₃N₄) photocatalyst activated by visible light, *ACS Catal.* 4 (2014) 774–780.
- [50] X. Wang, J. Zhou, H. Fu, W. Li, X. Fan, G. Xin, J. Zheng, X. Li, MOF derived catalysts for electrochemical oxygen reduction, *J. Mater. Chem. A* 2 (2014) 14064–14070.
- [51] D. Dolat, N. Quici, E. Kusiak-Nejman, A.W. Morawski, G. Li Puma, One-step, hydrothermal synthesis of nitrogen, carbon co-doped titanium dioxide (N,CTiO₂) photocatalysts. Effect of alcohol degree and chain length as carbon dopant precursors on photocatalytic activity and catalyst deactivation, *Appl. Catal. B Environ.* 115–116 (2012) 81–89.
- [52] Y.-X. Ye, C. Wen, J. Pan, J.-W. Wang, Y.-J. Tong, S. Wei, Z. Ke, L. Jiang, F. Zhu, N. Zhou, M. Zhou, J. Xu, G. Ouyang, Visible-light driven efficient overall H₂O₂ production on modified graphitic carbon nitride under ambient conditions, *Appl. Catal. B Environ.* 285 (2021), 119726.
- [53] A. Cabrera Reina, L. Santos-Juanes, J.L. García Sánchez, J.L. Casas López, M. I. Maldonado Rubio, G. Li Puma, J.A. Sánchez Pérez, Modelling the photo-Fenton oxidation of the pharmaceutical paracetamol in water including the effect of photon absorption (VRPA), *Appl. Catal. B Environ.* 166–167 (2015) 295–301.
- [54] S.-W. Nam, C. Jung, H. Li, M. Yu, J.R.V. Flora, L.K. Boateng, N. Her, K.-D. Zoh, Y. Yoon, Adsorption characteristics of diclofenac and sulfamethoxazole to graphene oxide in aqueous solution, *Chemosphere* 136 (2015) 20–26.
- [55] Y. Jia, L. Zhou, C. Ferronato, X. Yang, A. Salvador, C. Zeng, J.-M. Chovelon, Photocatalytic degradation of atenolol in aqueous titanium dioxide suspensions: kinetics, intermediates and degradation pathways, *J. Photochem. Photobiol. A-Chem.* 254 (2013) 35–44.
- [56] P.L. Brezonik, J. Fulkerson-Brekken, Nitrate-induced photolysis in natural waters: controls on concentrations of hydroxyl radical photo-intermediates by natural scavenging agents, *Environ. Sci. Technol.* 32 (1998) 3004–3010.
- [57] OECD, Test No. 202: Daphnia sp. Acute Immobilisation Test, 2004.
- [58] P. Chen, Q. Zhang, Y. Su, L. Shen, F. Wang, H. Liu, Y. Liu, Z. Cai, W. Lv, G. Liu, Accelerated photocatalytic degradation of diclofenac by a novel CQDs/BiOOH hybrid material under visible-light irradiation: dechlorination, detoxicity, and a new superoxide radical model study, *Chem. Eng. J.* 332 (2018) 737–748.
- [59] C. Martinez, M. Canle L, M.I. Fernandez, J.A. Santaballa, J. Faria, Aqueous degradation of diclofenac by heterogeneous photocatalysis using nanostructured materials, *Appl. Catal. B-Environ.* 107 (2011) 110–118.
- [60] W. Liu, Y. Li, F. Liu, W. Jiang, D. Zhang, J. Liang, Visible-light-driven photocatalytic degradation of diclofenac by carbon quantum dots modified porous g-C₃N₄: mechanisms, degradation pathway and DFT calculation, *Water Res.* 151 (2019) 8–19.
- [61] H. Yu, E. Nie, J. Xu, S. Yan, W.J. Cooper, W. Song, Degradation of diclofenac by advanced oxidation and reduction processes: kinetic studies, degradation pathways and toxicity assessments, *Water Res.* 47 (2013) 1909–1918.
- [62] L.A. Perez-Estrada, S. Malato, W. Gernjak, A. Agüera, E.M. Thurman, I. Ferrer, A. R. Fernandez-Alba, Photo-fenton degradation of diclofenac: Identification of main intermediates and degradation pathway, *Environ. Sci. Technol.* 39 (2005) 8300–8306.
- [63] Y. Rao, Y. Zhang, F. Han, H. Guo, Y. Huang, R. Li, F. Qi, J. Ma, Heterogeneous activation of peroxymonosulfate by LaFeO₃ for diclofenac degradation: DFT-assisted mechanistic study and degradation pathways, *Chem. Eng. J.* 352 (2018) 601–611.
- [64] H.S. Wahab, T. Bredow, S.M. Aliwi, A computational study on the adsorption and ring cleavage of para-chlorophenol on anatase TiO₂ surface, *Surf. Sci.* 603 (2009) 664–669.